Check for updates

Received: 25 February 2023 | Revised: 4 October 2023 | Accepted: 4 October 2023

DOI: 10.1002/mp.16803

RESEARCH ARTICLE

MEDICAL PHYSICS

A finite element method for modeling diffusion of alpha-emitting particles in tissue

Irene P. Zhang | **Gilad N. Cohen** | **Antonio L. Damato**

Department of Medical Physics, Memorial Sloan Kettering Cancer Center, New York City, New York, USA

Correspondence
Antonio L. Damato, Department of Medical Physics, Memorial Sloan Kettering Cancer Center, New York City, NY 10065, USA.
Email: damatoa@mskcc.org

Funding information
Alpha Tau Medical, Grant/Award Number: SK2020_0598; NCI, Grant/Award Number: P 30 CA008748

Abstract

Background: Diffusing alpha-emitters Radiation Therapy ("DaRT") is a promising new modality for the treatment of solid tumors. Interstitial sources containing ^{224}Ra are inserted into the tumor, producing alpha particles via the decay of ^{224}Ra and its daughters. The alpha particles are able to produce a "kill region" of several mm due to the diffusion of the alpha-emitting atoms. The Diffusion-Leakage (D-L) model has been proposed to describe the movement of the alpha-emitters used in DaRT in tumor tissue.

Purpose: To date, estimating the dose delivered under the D-L model has been accomplished with numerical solutions based on finite difference methods, namely DART1D and DART2D, as well as with asymptotic expressions for the long time limit. The aim of this work is to develop a flexible method of finite elements for solving the D-L model and to validate prior solutions of the D-L model.

Methods: We develop a two-dimensional finite element solution to the D-L model implemented using the FEniCS software library. Our approach solves the variational formulation of the D-L equations on an unstructured mesh of triangular Lagrangian elements. We calculate the local dose in the mid- and axial planes of the source and validate our results against the one- and two-dimensional solutions obtained using the previously proposed numerical scheme, DART1D and DART2D. We use our model to estimate the change in dose in the source midplane as a function of the physical parameters used in the D-L model.

Results: The local dose at the end of a 30 day treatment period estimated by our numerical method differs from DART1D and DART2D by less than 1% in the source midplane and less than 3% along the source axis over clinically relevant distances, with the largest discrepancies in high gradient areas where the Finite Element Method (FEM) mesh has a higher element density. We find that within current experimentally estimated ranges for D-L model parameters, the dose in the source midplane at a distance of 2 mm can vary by over a factor of 3.

Conclusions: The 2D finite element model reproduces the calculated dose obtained with DART1D and DART2D under the assumptions D-L model. The variation in predicted dose within current experimental ranges for model parameters suggests the necessity of further studies to better determine their statistical distributions. Finally, the FEM model can be used to calculate dose from DaRT in a variety of realistic 2D geometries beyond the D-L model.

KEYWORDS
alpha particles, diffusion, finite element

 © 2023 American Association of Physicists in Medicine.

1 | INTRODUCTION

The efficacy of Diffusing alpha-emitters Radiation Therapy ("DaRT") in treating bulky tumors has been due to multiple advantageous properties of alpha particles.[1–4] Alpha particles have a high linear energy transfer (LET) and produce almost equal levels of lethal DNA damage in hypoxic cells as in oxic cells. Furthermore, their short range allows for the sparing of healthy tissue. The alpha particle sources in DaRT are thin metallic cylinders carrying a few μCi of ^{224}Ra activity that are inserted intratumorally.[5] The ^{224}Ra decays, releasing daughter species (^{220}Rn, ^{216}Po, ^{212}Pb, ^{212}Bi, ^{212}Po, ^{208}Tl, and ^{208}Pb) from the source surface by recoil. Even after the daughters have expended their initial kinetic energy, they continue to move through tissue via diffusive and convective processes, releasing alpha and beta particles in subsequent decays. The alpha generating decays are ^{220}Rn to ^{216}Po, ^{216}Po to ^{212}Pb, ^{212}Bi to ^{208}Tl, and ^{212}Po to ^{208}Pb (Figure 1). The "kill region" surrounding the source is typically a few mm in radius.[1]

DaRT has been studied extensively in mice, and more recently, in clinical trials. A first-in-human study[5] of squamous cell carcinomas saw a complete response in 22/28 lesions after 30 days, while 6/28 lesions had a partial response. In one patient, an abscopal effect was observed. No toxicities above grade 2 were observed, and 90% of pain and grade 2 skin ulcerations in patients were resolved within 3 to 5 weeks. Additionally, DaRT has been shown in preclinical studies to increase tumor response when combined with chemotherapy[7–9] and immunotherapy.[10–13]

The "Diffusion-Leakage (D-L) Model" has been proposed as a simple model to describe the dose deposition in tissue from DaRT.[14] Under the D-L model, all particle motion can be attributed to diffusion, described by a global diffusion constant that is constant in space and time and depends on the particle species and surrounding medium. Any convection is assumed to have a short correlation length so that the motion is effectively diffusive. The removal of ^{212}Pb and ^{212}Bi from the tumor via blood vessels is assumed to occur at a constant rate throughout the tumor. It has been shown previously[14] that modeling the motion of ^{220}Rn, ^{212}Pb, and ^{212}Bi is sufficient to describe the distribution of ^{224}Ra daughters within the tumor. Closed form solutions of the D-L model for limiting cases have been proposed,[14] as well as numerical schemes for solving the D-L equations in one and two dimensions,[15,16] known as DART1D and DART2D, respectively. The numerical schemes have been used to develop source placement recommendations for treatment planning.[16]

We present an alternative approach to numerically solving the D-L model using finite elements. We reformulate the D-L model as a variational problem, which we then solve using Galerkin methods on an unstructured mesh. We independently validate the results of DART1D and DART2D to within 1% in the source midplane and 3% along the source axis. Our approach allows for local mesh refinement in high gradient regions where a higher element density may be advantageous, as well as easy incorporation of time dependent and spatially inhomogeneous model parameters, the latter of which will be the subject of future work. The ability to model nonuniform tissue geometries is necessary for dose calculations in more realistic scenarios.[14]

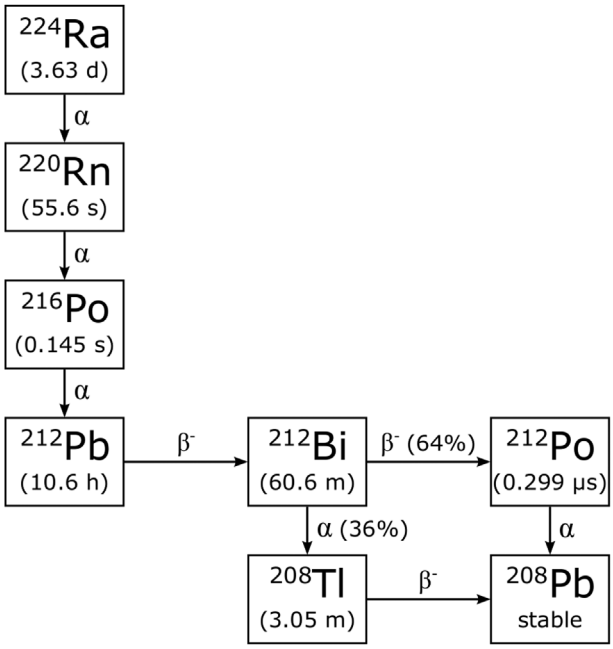

FIGURE 1 Decay chain of ^{224}Ra. Data taken from NuDat 3 database.[6]

2 | METHODS

2.1 | The D-L model

The migration of the ^{224}Ra daughters can be described by a set of coupled diffusion-advection equations. We simulate the dose delivered by a single DaRT source according to the (D-L) model.[14] The D-L model has the following assumptions:

1. The movement of atoms is dominated by diffusion. The contribution of advective terms is minimal.
2. The tissue surrounding the source is constant in space and time so that the diffusion-related model parameters are constant as well.
3. It is sufficient to model the diffusion of ^{220}Ra, ^{212}Pb, and ^{212}Bi. Their respective daughter species are assumed to be in local secular equilibrium with the parent.
4. The migration of ^{212}Pb can be described by a single diffusion coefficient averaged over all molecular species.

24734209, 0, Downloaded from https://aapm.onlinelibrary.wiley.com/doi/10.1002/mp.16803 by Eliran Ron - Cochrane Israel , Wiley Online Library on [07/11/2023]. See the Terms and Conditions (https://onlinelibrary.wiley.com/terms-and-conditions) on Wiley Online Library for rules of use; OA articles are governed by the applicable Creative Commons License

5. The clearance of ^{212}Pb atoms from the tumor via blood vessels can be described by a constant finite clearance rate.
6. ^{212}Bi is similarly cleared from the tumor, but this is a second order effect.
7. ^{220}Rn fully decays inside the tumor without being cleared.

Under the above assumptions, the number densities of ^{220}Rn, ^{212}Pb, and ^{212}Bi at point $\mathbf{r} \equiv (x, y, z)$ and time t in a volume of interest can be calculated using the D-L model equations:

$$\frac{\partial n_{Rn}}{\partial t} = D_{Rn}\nabla^2 n_{Rn} - \lambda_{Rn} n_{Rn} \tag{1}$$

$$\frac{\partial n_{Pb}}{\partial t} = D_{Pb}\nabla^2 n_{Pb} + \lambda_{Rn} n_{Rn} - \lambda_{Pb} n_{Pb} - \alpha_{Pb} n_{Pb} \tag{2}$$

$$\frac{\partial n_{Bi}}{\partial t} = D_{Bi}\nabla^2 n_{Bi} + \lambda_{Pb} n_{Pb} - \lambda_{Bi} n_{Bi} - \alpha_{Bi} n_{Bi} \tag{3}$$

where n_{Rn}, n_{Pb}, n_{Bi} are the number densities, D_{Rn}, D_{Pb}, D_{Bi} are the diffusion coefficients, and $\lambda_{Rn}, \lambda_{Pb}, \lambda_{Bi}$ are the decay rates of ^{220}Rn, ^{212}Pb, and ^{212}Bi, respectively, and α_{Pb} and α_{Bi} are the clearance rates of ^{212}Pb, and ^{212}Bi, respectively. The terms in Equations 2 and 3 involving the number densities of the parent particle provide the source component due to the decay of the parent. For ^{220}Rn and ^{212}Pb, there is an additional source due to direct desorption from the surface of the source. This influx of particles can be described as a Neumann boundary condition at the source wall. No particles are released at the top and bottom surfaces of the source.

We consider a cylindrical source of radius R_0 and length l situated at the origin and lying along the z-axis. We have the following boundary condition at $r = \sqrt{x^2 + y^2} = R_0$[15]:

$$\frac{\partial n_{Rn}}{\partial n} = P_{des}(Rn)\frac{\Gamma^{src}_{Ra}(0)}{2\pi R_0 l D_{Rn}} e^{-\lambda_{Ra} t} \tag{4}$$

$$\frac{\partial n_{Pb}}{\partial n} = (P_{des}(Pb) - P_{des}(Rn))\frac{\Gamma^{src}_{Ra}(0)}{2\pi R_0 l D_{Pb}} e^{-\lambda_{Ra} t} \tag{5}$$

$$\frac{\partial n_{Bi}}{\partial n} = 0, \tag{6}$$

where $\lambda_R a$ is the decay rate of ^{224}Ra and $\Gamma^{src}_{Ra}(0)$ is the initial activity on the source. The desorption probabilities of ^{220}Rn and ^{212}Pb, $P_{des}(Rn)$ and $P_{des}(Pb)$, give the respective probabilities of a ^{220}Rn or ^{212}Pb atom being emitted from the source following a decay of ^{224}Ra. The derivative in the outward normal direction to the boundary, $\frac{\partial n_k}{\partial n}$, can be related to the radial component of the diffusion current, j_k, by $j_k = D_k \frac{\partial n_k}{\partial n}$, where k is ^{220}Rn, ^{212}Pb, or ^{212}Bi. Far away from the source ($r \to \infty$), we impose the Dirichlet boundary conditions

$$n_k = 0 \tag{7}$$

for $k = {}^{220}$Rn, ^{212}Pb, and ^{212}Bi.

Following Heger et al.,[15] we define the diffusion lengths

$$L_{Rn} = \sqrt{\frac{D_{Rn}}{\lambda_{Rn} - \lambda Ra}} \tag{8}$$

$$L_{Pb} = \sqrt{\frac{D_{Pb}}{\lambda_{Pb} + \alpha_{Pb} - \lambda_{Ra}}} \tag{9}$$

$$L_{Bi} = \sqrt{\frac{D_{Bi}}{\lambda_{Bi} + \alpha_{Bi} - \lambda_{Bi}}}, \tag{10}$$

which combine the diffusion coefficients, decay rates, and clearance rates into a single parameter which describes the spatial spread of ^{220}Rn, ^{212}Pb, and ^{212}Bi, respectively.

Once the number densities n_{Rn}, n_{Pb}, and n_{Bi} are known, the local component of the dose due to alpha decay of ^{220}Rn and ^{216}Po and of ^{212}Bi and ^{212}Po can be calculated by

$$Dose_\alpha(RnPo;\ r, z, t) = \frac{E_\alpha(RnPo)}{\rho}\int_0^t \lambda_{Rn} n_{Rn}(r, z, t')dt' \tag{11}$$

$$Dose_\alpha(BiPo;\ r, z, t) = \frac{E_\alpha(BiPo)}{\rho}\int_0^t \lambda_{Bi} n_{Bi}(r, z, t')dt' \tag{12}$$

where $E_\alpha(RnPo)$ is the total alpha particle energy of ^{220}Rn and ^{216}Po, $E_\alpha(BiPo)$ is the weighted-average alpha particle energy of ^{212}Bi and ^{212}Po, and ρ is the tissue density. Equations 11–12 assume that because the range of the alpha particles is much smaller than the diffusion lengths, the energy of the alpha particles is deposited in the immediate vicinity of the decay.[14]

2.2 | Finite element formulation

The use of finite element methods (FEMs) to solve systems of partial differential equations with physical origins is well-documented.[17,18] We present here a brief sketch of the principles of FEM as relevant to the current work. We solve Equations 1–3 in two domain geometries. First, we consider the midplane ($z = 0$ mm) geometry, analogous to one-dimensional finite difference scheme proposed in Heger et al.[15] Next, we show preliminary dose calculations in the axial plane ($x = 0$ mm), analogous to the previously proposed two-dimentional finite difference scheme.[15]

24734209, 0, Downloaded from https://aapm.onlinelibrary.wiley.com/doi/10.1002/mp.16803 by Eliran Ron - Cochrane Israel , Wiley Online Library on [07/11/2023]. See the Terms and Conditions (https://onlinelibrary.wiley.com/terms-and-conditions) on Wiley Online Library for rules of use; OA articles are governed by the applicable Creative Commons License

2.2.1 | Dose profile in source midplane

We solve the D-L equations in two dimensions over a 14 mm-by-14 mm domain in the midplane of the source ($z = 0$ mm). We exclude the circular source area and consider the source surface as a boundary. We define the following notation for the domain and boundaries:

$$\Omega\text{: solution domain} \tag{13}$$

$$\partial\Omega_{source}\text{: source surface} \tag{14}$$

$$\partial\Omega_{edge}\text{: outside boundary} \tag{15}$$

Equations 1–3 are the strong form expression of our diffusion process and can be written as an operator on the solution vector $\mathbf{n} = (n_{Rn}, n_{Pb}, n_{Bi})$.

$$\mathbf{F}(\mathbf{n}(\mathbf{r})) = \mathbf{0}\ \forall \mathbf{r} \in \Omega. \tag{16}$$

We relax our requirements for the approximate solution $\mathbf{n}(\mathbf{r})$ so that it no longer needs to satisfy Equation 16, but instead satisfies the variational form[19]

$$\mathbf{F}(\mathbf{n}, \mathbf{v}) = \int_\Omega \mathbf{F}(\mathbf{n}) \cdot \mathbf{v} dA = 0\ \forall \mathbf{v} \in \mathbf{V}, \tag{17}$$

where $\mathbf{v} = (v_{Rn}, v_{Pb}, v_{Bi})$ is a vector of test functions, and $\mathbf{V} = \hat{V} \times \hat{V} \times \hat{V}$, where $\hat{V}$ is a suitable subspace of the space of continuous functions.[18] We require that $\mathbf{v}$ vanishes on Ω_{edge}, making the solution is exact on the boundaries. We further replace the time derivative with a backward Euler discretization.[17] At time step p,

$$\begin{aligned}
&\int_\Omega \left(\frac{n_{Rn}^p - n_{Rn}^{p-1}}{\Delta t} - D_{Rn}\nabla^2 n_{Rn}^p + \lambda_{Rn} n_{Rn}^p \right) v_{Rn} dA \\
&+ \int_\Omega \left(\frac{n_{Pb}^p - n_{Pb}^{p-1}}{\Delta t} - D_{Pb}\nabla^2 n_{Pb}^p - \lambda_{Rn} n_{Rn}^p \right. \\
&\left. + \lambda_{Pb} n_{Pb}^p + \alpha_{Pb} n_{Pb}^p \right) v_{Pb} dA + \int_\Omega \left(\frac{n_{Bi}^p - n_{Bi}^{p-1}}{\Delta t} \right. \\
&\left. - D_{Bi}\nabla^2 n_{Bi}^p - \lambda_{Pb} n_{Pb}^p + \lambda_{Bi} n_{Bi}^p + \alpha_{Bi} n_{Bi}^p \right) v_{Bi} dA = 0,
\end{aligned} \tag{18}$$

where Δt is the time step size and $\mathbf{n}^p$ is the solution at the p-th time step. The differential element dA indicates a two-dimensional volume integral over Ω. Integrating the terms containing $D_k \nabla^2 n_k$ by parts, we obtain

$$\begin{aligned}
\mathbf{F}(\mathbf{n}, \mathbf{v}) = &\int_\Omega \left(\frac{n_{Rn}^p - n_{Rn}^{p-1}}{\Delta t} + \lambda_{Rn} n_{Rn}^p \right) v_{Rn} dA \\
&+ \int_\Omega D_{Rn} \nabla n_{Rn}^p \cdot \nabla v_{Rn} dA \\
&+ \int_\Omega \left(\frac{n_{Pb}^p - n_{Pb}^{p-1}}{\Delta t} - \lambda_{Rn} n_{Rn}^p + \lambda_{Pb} n_{Pb}^p + \alpha_{Pb} n_{Pb}^p \right) \\
&\times v_{Pb} dA + \int_\Omega D_{Pb} \nabla n_{Pb}^p \cdot \nabla v_{Pb} dA \\
&+ \int_\Omega \left(\frac{n_{Bi}^p - n_{Bi}^{p-1}}{\Delta t} - \lambda_{Pb} n_{Pb}^p + \lambda_{Bi} n_{Bi}^p + \alpha_{Bi} n_{Bi}^p \right) \\
&\times v_{Bi} dA + \int_\Omega D_{Bi} \nabla n_{Bi}^p \cdot \nabla v_{Bi} dA \\
&- \int_{\partial\Omega_{source}} D_{Rn} j_{Rn} v_{Rn} ds - \int_{\partial\Omega_{source}} D_{Pb} j_{Pb} v_{Pb} ds = 0,
\end{aligned} \tag{19}$$

where we have used the Neumann boundary conditions 4–6 to substitute for $\frac{\partial n_x}{\partial n}$ in the line integrals over $\partial\Omega_{source}$. Because $\mathbf{v}$ must vanish on the boundary where the exact solution is known, the integrals over $\partial\Omega_{edge}$ vanish as well. The solution to Equation 19 subject to the Dirichlet boundary conditions in Equation 7 approximates the solution to Equations 1–3.

By separating terms that depend on $\mathbf{n}^p$ and $\mathbf{v}$ from terms that depend only on $\mathbf{v}$, we may rewrite Equation 19 in the form

$$a(\mathbf{n}^p, \mathbf{v}) = L(\mathbf{v}). \tag{20}$$

where the bilinear form $a(\mathbf{n}, \mathbf{v})$ and linear form $L(\hat{v})$[18] are given by

$$\begin{aligned}
a(\mathbf{n}^p, \mathbf{v}) = &\int_\Omega \left(\frac{n_{Rn}^p}{\Delta t} + \lambda_{Rn} n_{Rn}^p \right) v_{Rn} dA + \int_\Omega D_{Rn} \nabla n_{Rn}^p \cdot \nabla v_{Rn} dA \\
&+ \int_\Omega \left(\frac{n_{Pb}^p}{\Delta t} - \lambda_{Rn} n_{Rn}^p + \lambda_{Pb} n_{Pb}^p + \alpha_{Pb} n_{Pb}^p \right) v_{Pb} dA \\
&+ \int_\Omega D_{Pb} \nabla n_{Pb}^p \cdot \nabla v_{Pb} dA \\
&+ \int_\Omega \left(\frac{n_{Bi}^p}{\Delta t} - \lambda_{Pb} n_{Pb}^p + \lambda_{Bi} n_{Bi}^p + \alpha_{Bi} n_{Bi}^p \right) v_{Bi} dA \\
&+ \int_\Omega D_{Bi} \nabla n_{Bi}^p \cdot \nabla v_{Bi} dA
\end{aligned} \tag{21}$$

$$\begin{aligned}
L(\mathbf{v}) = &\int_\Omega \frac{n_{Rn}^{p-1}}{\Delta t} v_{Rn} dA + \int_\Omega \frac{n_{Pb}^{p-1}}{\Delta t} v_{Pb} dA + \int_\Omega \frac{n_{Bi}^{p-1}}{\Delta t} v_{Bi} dA \\
&+ \int_{\partial\Omega_{source}} D_{Rn} j_{Rn} v_{Rn} ds + \int_{\partial\Omega_{source}} D_{Pb} j_{Pb} v_{Pb} ds.
\end{aligned} \tag{22}$$

To obtain the space-discretized variational problem, we divide the domain into triangular elements that comprise a mesh. Similarly, we make an ansatz for the discrete solution at time step p,[17]

$$\left(n_{Rn}^p, n_{Pb}^p, n_{Bi}^p \right) = \sum_j^N U_j^p (\phi_j, \psi_j, \chi_j), \tag{23}$$

24734209, 0, Downloaded from https://aapm.onlinelibrary.wiley.com/doi/10.1002/mp.16803 by Eliran Ron - Cochrane Israel , Wiley Online Library on [07/11/2023]. See the Terms and Conditions (https://onlinelibrary.wiley.com/terms-and-conditions) on Wiley Online Library for rules of use; OA articles are governed by the applicable Creative Commons License

where $\{(\phi_i, \psi_i, \chi_i)\}_i^N$ comprise a set of suitably chosen basis functions spanning the solution space. In our case, we restrict our solution space to continuous piecewise linear functions, and follow the Galerkin method so that the test function space $\hat{V}$ has the same set of basis functions as the corresponding solution space,[18] namely, the 2D linear Lagrange nodal basis. This basis consists of hat functions h_i where h_i has unit value at the i-th mesh node and is zero at all other nodes.[17] Substituting equation into Equations 21 and 22 and taking $(v_{Rn}, v_{Pb}, v_{Bi}) = (\phi_i, \psi_i, \chi_i)$ for $i = 1, \ldots, N$, we obtain for each time step a linear system of the form

$$AU^p = b \tag{24}$$

where

$$\begin{aligned} A_{ij} = &\int_\Omega \left(\frac{\phi_j}{\Delta t} + \lambda_{Rn}\phi_j\right)\phi_i dA + \int_\Omega D_{Rn}\nabla\phi_j \cdot \nabla\phi_i dA \\ &+ \int_\Omega \left(\frac{\psi_j}{\Delta t} - \lambda_{Rn}\phi_j + \lambda_{Pb}\psi_j + \alpha_{Pb}\psi_j^p\right)\psi_i dA \\ &+ \int_\Omega D_{Pb}\nabla\psi_j \cdot \nabla\psi_i dA \\ &+ \int_\Omega \left(\frac{\chi_j}{\Delta t} - \lambda_{Pb}\psi_j + \lambda_{Bi}\chi_j + \alpha_{Bi}\chi_j\right)\chi_i dA \\ &+ \int_\Omega D_{Bi}\nabla\chi_j \cdot \nabla\chi_i dA \end{aligned} \tag{25}$$

$$\begin{aligned} b_i = &\int_\Omega \frac{n_{Rn}^{p-1}}{\Delta t}\phi_i dA + \int_\Omega \frac{n_{Pb}^{p-1}}{\Delta t}\psi_i dA + \int_\Omega \frac{n_{Bi}^{p-1}}{\Delta t}\chi_i dA \\ &+ \int_{\partial\Omega_{source}} D_{Rn} j_{Rn}\phi_i ds + \int_{\partial\Omega_{source}} D_{Pb} j_{Pb}\psi_i ds. \end{aligned} \tag{26}$$

Equation 24 can be solved for U^p using standard linear solvers. In our case, we use lower-upper (LU) decomposition[17] as implemented in the FEniCS library.

2.2.2 | Dose profile in axial plane

In addition to the source midplane, we also solve the D-L equations in the plane intersecting the source along its axis. As before, the midpoint of the source is situated at the origin. Taking advantage of the axial symmetry of the problem, the domain extends in the radial direction from $r = 0$ to $r = 7$ mm and in the axial direction from $z = -10$ to $z = 10$ mm so that $|\max(z)| \gg l/2$, where l is the source length. In this case, we require that $\partial n_x/\partial n = 0$ at the top and bottom surfaces of the source and at $r = 0$ for $|z| > l/2$. To incorporate the radial symmetry into the FEniCS variational statement, we recast the D-L equations into cylindrical coordinates:

$$\frac{\partial n_{Rn}}{\partial t} = D_{Rn}\left[\frac{1}{r}\frac{\partial}{\partial r}\left(r\frac{\partial n_{Rn}}{\partial r}\right) + \frac{\partial^2 n_{Rn}}{\partial z^2}\right] - \lambda_{Rn} n_{Rn} \tag{27}$$

$$\begin{aligned} \frac{\partial n_{Pb}}{\partial t} = &D_{Pb}\left[\frac{1}{r}\frac{\partial}{\partial r}\left(r\frac{\partial n_{Pb}}{\partial r}\right) + \frac{\partial^2 n_{Pb}}{\partial z^2}\right] \\ &+\lambda_{Rn} n_{Rn} - (\lambda_{Pb} + \alpha_{Pb}) n_{Pb} \end{aligned} \tag{28}$$

$$\begin{aligned} \frac{\partial n_{Bi}}{\partial t} = &D_{Bi}\left[\frac{1}{r}\frac{\partial}{\partial r}\left(r\frac{\partial n_{Bi}}{\partial r}\right) + \frac{\partial^2 n_{Bi}}{\partial z^2}\right] \\ &+\lambda_{Pb} n_{Pb} - (\lambda_{Bi} + \alpha_{Bi}) n_{Bi} \end{aligned} \tag{29}$$

As in Equation 17, we take the inner product with our test functions to obtain the variational form, and we use the cylindrical area element $rdrdz$ in the integration over Ω. The resulting variational statement is

$$\begin{aligned} \mathbf{F}(\mathbf{n}, \mathbf{v}) = &\int_\Omega \left(\frac{n_{Rn}^p - n_{Rn}^{p-1}}{\Delta t} + \lambda_{Rn} n_{Rn}^p\right) v_{Rn} r dA \\ &+ \int_\Omega D_{Rn}\nabla n_{Rn}^p \cdot \nabla v_{Rn} r dA \\ &+ \int_\Omega \left(\frac{n_{Pb}^p - n_{Pb}^{p-1}}{\Delta t} - \lambda_{Rn} n_{Rn}^p + \lambda_{Pb} n_{Pb}^p + \alpha_{Pb} n_{Pb}^p\right) \\ &\times v_{Pb} r dA + \int_\Omega D_{Pb}\nabla n_{Pb}^p \cdot \nabla v_{Pb} r dA \\ &+ \int_\Omega \left(\frac{n_{Bi}^p - n_{Bi}^{p-1}}{\Delta t} - \lambda_{Pb} n_{Pb}^p + \lambda_{Bi} n_{Bi}^p + \alpha_{Bi} n_{Bi}^p\right) \\ &\times v_{Bi} r dA + \int_\Omega D_{Bi}\nabla n_{Bi}^p \cdot \nabla v_{Bi} r dA \\ &- \int_{\partial\Omega_{source}} D_{Rn} j_{Rn} v_{Rn} r ds \\ &- \int_{\partial\Omega_{source}} D_{Pb} j_{Pb} v_{Pb} r ds = 0, \end{aligned} \tag{30}$$

and the corresponding matrix entries for A and b in Equation 24 are

$$\begin{aligned} A_{ij} = &\int_\Omega \left(\frac{\phi_j}{\Delta t} + \lambda_{Rn}\phi_j\right)\phi_i r dA + \int_\Omega D_{Rn}\nabla\phi_j \cdot \nabla\phi_i r dA \\ &+ \int_\Omega \left(\frac{\psi_j}{\Delta t} - \lambda_{Rn}\phi_j + \lambda_{Pb}\psi_j + \alpha_{Pb}\psi_j^p\right)\psi_i r dA \\ &+ \int_\Omega D_{Pb}\nabla\psi_j \cdot \nabla\psi_i r dA \\ &+ \int_\Omega \left(\frac{\chi_j}{\Delta t} - \lambda_{Pb}\psi_j + \lambda_{Bi}\chi_j + \alpha_{Bi}\chi_j\right)\chi_i r dA \\ &+ \int_\Omega D_{Bi}\nabla\chi_j \cdot \nabla\chi_i r dA \end{aligned} \tag{31}$$

24734209, 0, Downloaded from https://aapm.onlinelibrary.wiley.com/doi/10.1002/mp.16803 by Eliran Ron - Cochrane Israel , Wiley Online Library on [07/11/2023]. See the Terms and Conditions (https://onlinelibrary.wiley.com/terms-and-conditions) on Wiley Online Library for rules of use; OA articles are governed by the applicable Creative Commons License

TABLE 1 Mesh regions and densities for the midplane geometry.

Region	Density
$d > 1.15$ mm	145 elements/mm^2
0.15 mm $< d \leq 1.15$ mm	600 elements/mm^2
0.025 mm $< d \leq 0.15$ mm	1200 elements/mm^2
d ≤ 0.025 mm	19 200 elements/mm^2

Note: Mesh regions and densities for the midplane geometry.

TABLE 2 Mesh regions and densities for the axial geometry.

Region	Density
$d > 0.25$ mm	3300 elements/mm^2
0.01 mm $< d \leq 0.25$ mm	14 300 elements/mm^2
$d \leq 0.01$ mm	69 000 elements/mm^2

Note: Mesh regions and densities for the axial geometry.

$$b_i = \int_\Omega \frac{n_{Rn}^{p-1}}{\Delta t}\phi_i r dA + \int_\Omega \frac{n_{Pb}^{p-1}}{\Delta t}\psi_i r dA + \int_\Omega \frac{n_{Bi}^{p-1}}{\Delta t}\chi_i r dA + \int_{\partial\Omega_{source}} D_{Rn} j_{Rn}\phi_i r ds + \int_{\partial\Omega_{source}} D_{Pb} j_{Pb}\psi_i r ds. \quad (32)$$

Here we follow the FEniCS convention where $\nabla f(r,z) = (\frac{\partial f}{\partial r}, \frac{\partial f}{\partial z})$ and $dA = drdz$.

2.3 | Implementation in FEniCS

We use the FEniCS[20,21] Python library (version 2019.1.0) to solve the linear variational problem in Equation 19. FEniCS uses a domain specific language, the Unified Form Language (UFL) to define discretized variational problems. UFL allows the user to define finite elements, function spaces, and abstract variational expressions.

FEniCS includes a number of built-in finite element families. For this work, we use linear 2D Lagrange elements in line with our use of the Galerkin method in the previous section. Because we have a system of coupled equations, we make use of the MixedElement class to combine three elements, one for each of n_{Rn}, n_{Pb}, and n_{Bi}. Given a finite element and a mesh, we then define a FEniCS FunctionSpace on which to solve our variational problem, as described in Equation 19. We define **n** and **v** on the same FunctionSpace composed of mixed linear Lagrange elements, following the space discretization described in Section 2.2

The boundary conditions 4–6 create steep gradients close to the source surface. These gradients lead to spurious oscillations on the length scale of the element size if the elements are not sufficiently small. We use FEniCS' built-in mesh refinement tool to refine the mesh in iterative steps as a function the distance d from the internal boundary. Tables 1 and 2 list the element densities for the midplane and axial domain geometries.

FEniCS allows the user to designate a TrialFunction and a TestFunction, equivalent to **n** and **v**, which FEniCS can then parse in the variational expression. The abstract variational expressions in Equations 19 and 30 are written directly as an input to the linear solver.[19] FEniCS then separates the appropriate terms for $a(\mathbf{n}^p, \mathbf{v})$ and $L(\mathbf{v})$ in Equation 20.

At each time step, FEniCS solves the variational problem using the solution at the previous time step. The FEniCS Form Compiler (FCC) assembles the $N \times N$ finite element matrix A, where N is the number of elements, which is 440 052 for the mid-plane and 798 213 for the axial plane, respectively. We use the LU decomposition method as implemented in FEniCS to solve the linear system in Equation 24.

Once the number densities n_{Rn}, n_{Pb}, and n_{Bi} are obtained, the dose can be updated by[15]

$$Dose_\alpha^p(RnPo; x, y) = Dose_\alpha^{p-1}(RnPo; x, y) + \frac{E_\alpha(RnPo)}{\rho}\lambda_{Rn} n_{Rn}^p(x, y)\Delta t \quad (33)$$

$$Dose_\alpha^p(BiPo; x, y) = Dose_\alpha^{p-1}(BiPo; x, y) + \frac{E_\alpha(BiPo)}{\rho}\lambda_{Bi} n_{Bi}^p(x, y)\Delta t \quad (34)$$

Additionally, we use the relative change in the total alpha dose summed over the solution domain to implement adaptive time stepping. We set the minimum Δt to be 0.1 s and the maximum Δt to be 3600 s.

We benchmark our approach against DART1D and DART2D, numerical schemes for solving the D-L model in one and two dimensions, respectively, using a finite difference approach based on discretization of derivatives. A complete description of DART1D and DART2D is found in Heger et al.[15] We compare results for the number densities n_{Rn}, n_{Pb}, and n_{Bi}, as well as the ^{220}Rn+^{216}Po and ^{21}Bi/^{212}Po alpha dose components for a treatment length of $t = 30$ days.

Our results are an independent validation of DART1D and DART2D.

For the sake of comparison, we match the values of our problem parameters to Heger et al.[15] We use desorption probabilities $P_{des}(Rn) = 0.45$ and $P_{des}^{eff}(Rn) = 0.55$. The ^{220}Rn, ^{212}Pb, and ^{212}Bi diffusion lengths are $L_{Rn} = 0.3$ mm, $L_{Pb} = 0.6$ mm, and $L_{Bi} = 0.1 L_{Pb}$, within the typical range seen in the literature.[14] Finally, we assume the ^{212}Pb clearance rate α_{Pb} is equal to its decay rate λ_{Pb}, and set $\alpha_{Bi} = 0$ to zero as we consider the clearance of ^{212}Bi to be a secondary effect. Further discussion of the variability of calculated doses due to uncertainty in tissue parameters can be found in Section 4

24734209, 0, Downloaded from https://aapm.onlinelibrary.wiley.com/doi/10.1002/mp.16803 by Eliran Ron - Cochrane Israel , Wiley Online Library on [07/11/2023]. See the Terms and Conditions (https://onlinelibrary.wiley.com/terms-and-conditions) on Wiley Online Library for rules of use; OA articles are governed by the applicable Creative Commons License

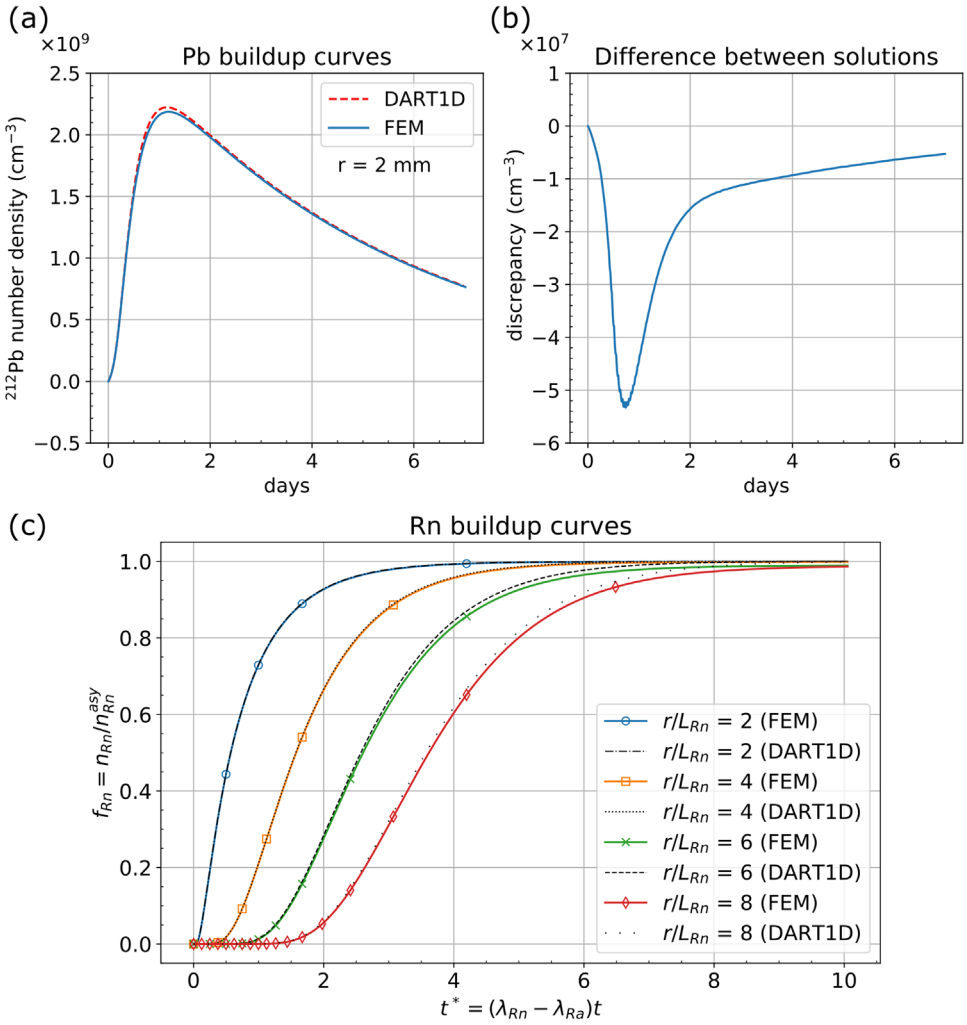

FIGURE 2 Number densities computed by our FEM implementation. (a) Left: Result for ^{212}Pb number density n_{Pb} plotted over 7 days using FEM (solid blue line) and using DART1D (dashed red line). Right: Discrepancy between the FEM and DART1D implementations. (b) Result for ^{220}Rn number density n_{Rn} using FEM (solid colored lines) and DART1D (dashed black lines). FEM, finite element method, DART, diffusing alpha-emitters radiation therapy.

3 | RESULTS

3.1 | Comparison with DART1D: Number density and alpha dose

Figure 2 shows a comparison between our results using the radial geometry and the DART1D results for n_{Pb} and n_{Rn} in the transient buildup stage before the number densities reach their respective asymptotic temporal behavior. The ^{212}Pb number density in panel (a) is plotted at a distance $r = 2$ mm from the central axis of the source. Our FEM results are systematically lower than the DART1D results, with a maximum discrepancy of 5.3×10^7 (panel (b)), equivalent to a change of 2.4%. Panel (c) shows the ^{220}Rn number density normalized by the asymptotic expression for n_{Rn}[15]

$$n_{Rn}^{asy}(r,t) = A_{Rn} K_0\left(\frac{r}{L_{Rn}}\right) e^{-\lambda_{Ra} t} \tag{35}$$

where A_{Rn} is a constant depending on the $P_{des}(Rn)$, L_{Rn}, the initial source activity and the source radius and length. The horizontal axis is normalized by the effective lifetime of ^{220}Rn, $1/(\lambda_{Rn} - \lambda_{Ra})$. We plot comparisons at a range of distances starting at $2L_{Rn}$ up to $8L_{Rn}$. Similar to our results for n_{Pb}, our results for n_{Rn} underestimate n_{Rn}, although for larger distances, the discrepancy can be partly attributed to imperfect matching between element node locations and the desired r value.

Figure 3 compares the alpha dose at the end of the 30 day treatment obtained by our method using the radial geometry described in Section 2.2.1 with that using DART1D. Panel (a) shows the ^{220}Rn+^{216}Po and ^{21}Bi/^{212}Po contributions to the alpha dose as a function of distance from the source axis. Like the DART1D solution, our solution shows edge effects due to the Dirichlet boundary conditions at the outer boundary of the domain, although the effect is more severe in our case. For distances less than 2 mm, our solution tends

24734209, 0, Downloaded from https://aapm.onlinelibrary.wiley.com/doi/10.1002/mp.16803 by Eliran Ron - Cochrane Israel , Wiley Online Library on [07/11/2023]. See the Terms and Conditions (https://onlinelibrary.wiley.com/terms-and-conditions) on Wiley Online Library for rules of use; OA articles are governed by the applicable Creative Commons License

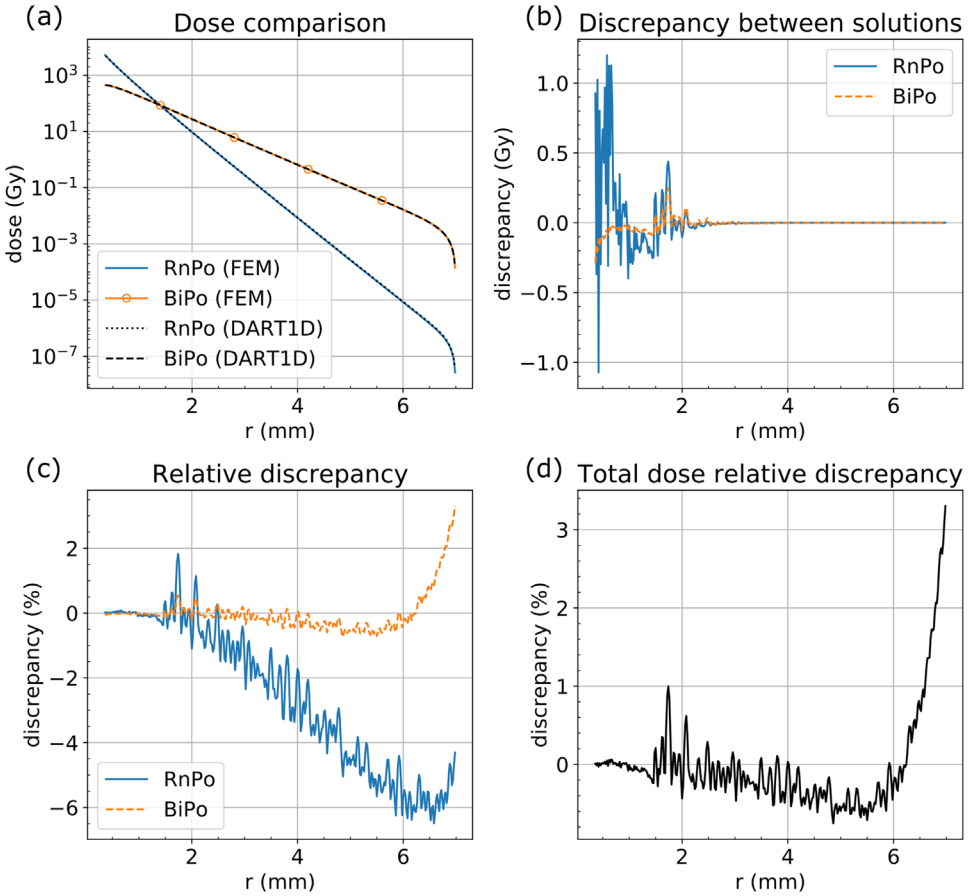

FIGURE 3 Comparison of the FEM and DART1D solutions for the ^{220}Rn+^{216}Po and ^{212}Bi/^{212}Po contributions to the alpha dose in the source midplane. (a) Dose result using FEM (solid lines) and DART1D (dashed lines). (b) Absolute discrepancy between our and the DART1D solutions for each component of the alpha dose. (c) Relative discrepancy between our solution and DART1D for each alpha dose component, where the normalization is done with respect to the DART1D solution. (d) Relative discrepancy for the total dose, including both components. FEM, finite element method, DART, diffusing alpha-emitters radiation therapy.

to overestimate the ^{220}Rn+^{216}Po dose compared to DART1D with a maximum discrepancy of 1.2 Gy, relative to a dose of over 1 kGy (panel (b)). Similarly, the discrepancy in the calculated ^{21}Bi/^{212}Po alpha doses has its maximum of −0.3 Gy at the source surface, where dose values are over 100 Gy. The minimal necessary dose for effective tumor killing was found to be 10 Gy in preclinical studies of SCC tumors in mice.[1] For both alpha dose contributions, a dose of 10 Gy is reached in the 2–3 mm range, in which the discrepancies are less than 0.15 Gy. Panel (c) shows the relative discrepancy between our results and the DART1D result $(Dose_{\alpha}^{FEM} - Dose_{\alpha}^{DART})/Dose_{\alpha}^{DART}$. For $r < 1.5$ mm, the relative discrepancies for both alpha dose components are on the order of 10^{-4}. At distances greater than 1.5 mm, where the element size increases dramatically, the relative discrepancy begins to increase, reaching a maximum of 6% underestimation for the ^{220}Rn+^{216}Po alpha dose and 0.6% underestimation for the ^{21}Bi/^{212}Po alpha dose, before the onset of edge effects about 1 mm from the outer boundary at 7 mm. We note that the dose values at the distances at which the relative discrepancies in ^{220}Rn+^{216}Po and ^{21}Bi/^{212}Po dose reach their maximum are less than 1 μGy and 0.1 Gy, respectively. Finally, in panel (d), we show the relative discrepancy for the total dose including both components. At clinically relevant distances of less than 3 mm, where there is appreciable alpha dose, the relative discrepancy is limited to less than 1%. Beyond 3 mm, the relative discrepancy reaches a maximum of 3.3% at 7 mm, where the solution is not reliable due to a large contribution from edge effects.

3.2 | Effect of varying diffusion lengths, clearance rates, and probabilities of desorption

We used the source midplane geometry to investigate how the dose profile changes when different values for the model parameters are used. Using the midplane geometry shortens the necessary computation compared to the axial geometry, and the resulting midplane dose is accurate to within 2% at clinically relevant distances of that obtained using the axial geometry (Figure S1), which takes into account the finite length

24734209, 0, Downloaded from https://aapm.onlinelibrary.wiley.com/doi/10.1002/mp.16803 by Eliran Ron - Cochrane Israel , Wiley Online Library on [07/11/2023]. See the Terms and Conditions (https://onlinelibrary.wiley.com/terms-and-conditions) on Wiley Online Library for rules of use; OA articles are governed by the applicable Creative Commons License

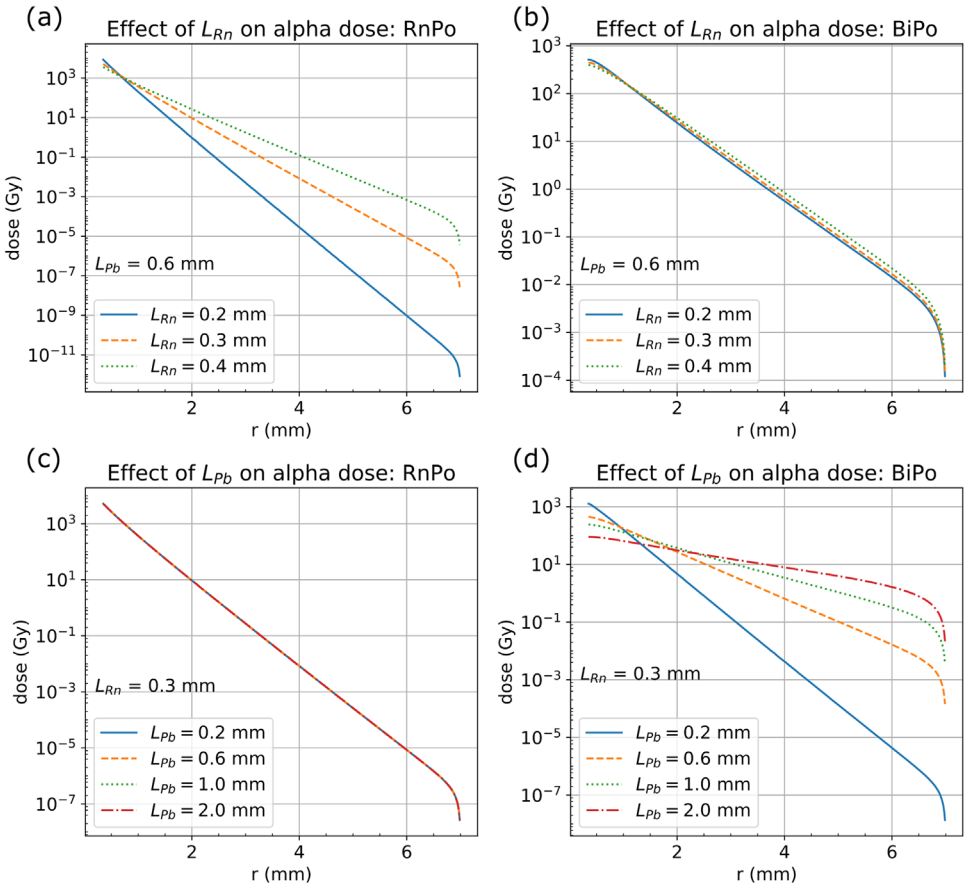

FIGURE 4 ^{220}Rn+^{216}Po and ^{21}Bi/^{212}Po contributions to the alpha dose for different values of L_{Rn} and L_{Pb}. (a)^{220}Rn+^{216}Po alpha dose for varying L_{Rn}. L_{Pb} is fixed at 0.6 mm. (b) Same as (a) for the ^{21}Bi/^{212}Po alpha dose. (c)^{220}Rn+^{216}Po alpha dose for varying L_{Pb}. L_{Rn} is fixed at 0.3 mm. (d) Same as (c) for the ^{21}Bi/^{212}Po alpha dose.

of the source. Figure 4 shows the radial alpha dose profile for a range of values of L_{Rn} and L_{Pb}. Typical ranges found in the literature for L_{Rn} and L_{Pb} are 0.2 to 0.4 mm and 0.2 to 2 mm, respectively.[1,14,22,23] As illustrated in panel (a), varying L_{Rn} from 0.2 to 0.4 mm while fixing L_{Pb} at 0.6 mm results in an increase by a factor of almost 30 in the ^{220}Rn+^{216}Po dose delivered at 2 mm, or half the recommended source spacing for treatment.[16] Over the same range of L_{Rn} values, the distance over which the dose remains above 10 Gy increases from 1.5 to 2.4 mm. A small effect with varying L_{Rn} is seen in the ^{21}Bi/^{212}Po alpha dose (panel (b)); the corresponding change in dose in this case is a factor of 1.27. The maximum distance to maintain 10 Gy of ^{21}Bi/^{212}Po alpha dose ranges from 2.4 to 2.6 mm. Combining both components, the total dose at 2 mm is larger for $L_{Rn} = 0.4$ mm than for $L_{Rn} = 0.2$ mm by a factor of 2.3. As expected, changing L_{Pb} has little to no effect on the ^{220}Rn+^{216}Po alpha dose, as the associated decays occur before the production of ^{212}Pb (panel (c)); the change is less than 0.05%. In contrast, the effect of increasing L_{Pb} from 0.2 to 2.0 mm with L_{Rn} fixed at 0.3 mm is to increase the calculated ^{21}Bi/^{212}Po alpha dose at 2 mm by a factor of 8. The distance at which 10 Gy is reached increases from 1.8 mm for $L_{Pb} = 0.2$ to 3.6 mm for $L_{Pb} = 2$ mm. Combining both components, the total dose at 2 mm is larger for $L_{Pb} = 1$ mm than for $L_{Pb} = 0.2$ mm by a factor of 3.3. These results support previous observations that optimal placement of sources is dependent on the diffusion properties of the tumor tissue.[15,16]

Although the clearance rate α_{Pb} is incorporated in the diffusion length L_{Pb}, the effect of varying α_{Pb}, while keeping L_{Pb} fixed at 0.6 mm, was investigated. The resulting dose in the seed midplane can be found in the Supporting Information. The range of values for α_{Pb} estimated from mouse experiments is $0.5\lambda_{Pb}$ to $2\lambda_{Pb}$.[14] This range corresponds to a <0.002% change in the ^{220}Rn+^{216}Po alpha particle dose at 2 mm (Figure S2(a)). For the ^{21}Bi/^{212}Po alpha dose, the dose resulting from $\alpha_{Pb} = 0.5\lambda_{Pb}$ is 1.95 times as large as the dose resulting from $\alpha_{Pb} = 2\lambda_{Pb}$ (Figure S2(b)). A dose of 10 Gy is reached at 2.67 mm for $\alpha_{Pb} = 0.5\lambda_{Pb}$ and at 2.32 mm for $\alpha_{Pb} = 2\lambda_{Pb}$. The ^{212}Bi clearance rate α_{Bi} is assumed to be zero in the D-L model.

The desorption probabilities $P_{des}(Rn)$ and $P_{des}(Pb)$ were found to have a much smaller effect on the alpha particle dose compared to the diffusion lengths. The estimated range of values for $P_{des}(Rn)$ is 0.35 to 0.45.[14] The change in dose at 2 mm across this

24734209, 0, Downloaded from https://aapm.onlinelibrary.wiley.com/doi/10.1002/mp.16803 by Eliran Ron - Cochrane Israel , Wiley Online Library on [07/11/2023]. See the Terms and Conditions (https://onlinelibrary.wiley.com/terms-and-conditions) on Wiley Online Library for rules of use; OA articles are governed by the applicable Creative Commons License

range is 29% for the ^{220}Rn+^{216}Po component and 5% for the ^{21}Bi/^{212}Po component (Figure S3(a)–(b)). The change in minimum distance at which 10 Gy is delivered is < 0.1 mm for both components, smaller than the achievable source placement accuracy in most clinical scenarios.[24] For $P_{des}(Pb)$, the estimated range of values is 0.5 to 0.6.[14] The corresponding change in dose at 2 mm from the source axis is $< 0.002\%$ for the ^{220}Rn+^{216}Po component and 16% for the ^{21}Bi/^{212}Po component (Figure S3(c)–(d)). The ^{21}Bi/^{212}Po component reaches 10 Gy at the same location to within 0.01 mm at both ends of the estimated range.

3.3 | Solution convergence

We show the convergence and stability of the midplane solution with element size. We use the dose at the end of the 30 day treatment period as a measure of solution convergence rather than the number densities n_{Rn}, n_{Pb}, and n_{Bi} because the clinically relevant quantity is the dose delivered. Furthermore, the accumulated dose incorporates both the temporal development (as it is an integral of the n_{Rn} and n_{Bi}) and the spatial variation of **n**. The largest contribution to the total element count is in the region closest to the source surface, $r \leq 0.375$ mm. This region is also most susceptible to large errors due to insufficiently small element size. We successively coarsen our mesh within each circular subdomain described in Section 2.3 until the element density inside matches that of the remainder of the problem domain. Once the entire domain has the same element density, we continue to decrease the number of elements until the number of mesh elements is roughly 1% of the original 440 052, an arbitrary cutoff to show the shape of the convergence plot. In Figure 5, we show the calculated dose in the midplane geometry at $r = 0.35$ mm (at the source surface), 1, 2, and 3 mm as a function of the number of mesh elements. The value obtained for the dose starts to flatten above 80 000 elements. At 440 052 elements, which is the number of elements used to obtain the results in this section, the dose is well into the flat portion of the curve at all four distances.

3.4 | Comparison with DART2D: alpha particle dose

The total alpha dose at the end of the 30 day treatment calculated using the axial plane geometry described in Section 2.2.2 is shown in Figure 6. The dose is largest around the source wall (but not the source ends where no diffusing isotopes are released), falling off rapidly with increasing distance and reaching 10 Gy between 2 and 3 mm. For small radial distances, the dose changes little along the z-direction until the source end is reached, but farther away, the isodose lines begin curving towards the source axis starting at around 2.5 mm from the source top and bottom. Panel (b) shows the the difference between the dose calculated using our method and the dose calculated using DART2D. Panel (c) shows this difference normalized by the DART2D dose values. The radial dose profile is taken at $z = 0$ mm, and axial dose profile is taken at $r = 0.35$ mm, the location of the source wall. The x-axis in panels (c) and (d) is distance from the boundary of the source, which is the source wall for the radial profile and the source top/bottom for the axial profile. Compared with DART2D, our solution shows a trend toward higher doses in the axial direction and lower doses in the radial direction at distances within 1 mm of the source. One explanation for the discrepancy between our solution and DART2D could be the difference in element size in this region. Aside from the domain boundaries, the location with the largest discrepancy in the axial dose is at the source ends, where the gradient is also the largest (Figure S4). The spacing between mesh nodes in the z-direction in DART2D is 0.05 mm, while the typical side length of each triangular mesh element in our implementation is less than 0.015 mm in the regions closest to the source. At distances greater than 3 mm, our dose estimation falls off more rapidly than DART2D because our domain is smaller, meaning that the onset boundary effects occurs at smaller distances. The systematic negative offset seen at closer distances could also be a result of the smaller domain size. Below 3 mm, the difference between our dose calculation and DART2D's is less than 0.25% in the radial direction and less than 3% in the axial direction.

4 | DISCUSSION

DaRT has been of great clinical interest.[4,5,25] Because its dose deposition mechanism is radically different than typical brachytherapy sources,[1,14] it is crucial to develop reliable methods of calculating the expected dose for clinical use. Dose calculation has been investigated by one research group[14–16] without independent validation. Given this is the only model in existence, it has been adopted in clinical trials even if lacking independent validation from other groups.[14,16] The D-L model is a simplified diffusive model and assumes the source is in an isotropic, time-independent medium, far away from any boundaries. In reality, the diffusion parameters likely vary in space with changing tissue health and degree of vasculature.[1] Additionally, many cancers for which DaRT may be effective,[5,25] such as cancers of the skin or head and neck, will need an approach that is able to model tissue-to-air boundaries. Finally, the success of any DaRT dose model, D-L and otherwise, depends on accurate determination of the diffusive properties of the source environment.

24734209, 0, Downloaded from https://aapm.onlinelibrary.wiley.com/doi/10.1002/mp.16803 by Eliran Ron - Cochrane Israel , Wiley Online Library on [07/11/2023]. See the Terms and Conditions (https://onlinelibrary.wiley.com/terms-and-conditions) on Wiley Online Library for rules of use; OA articles are governed by the applicable Creative Commons License

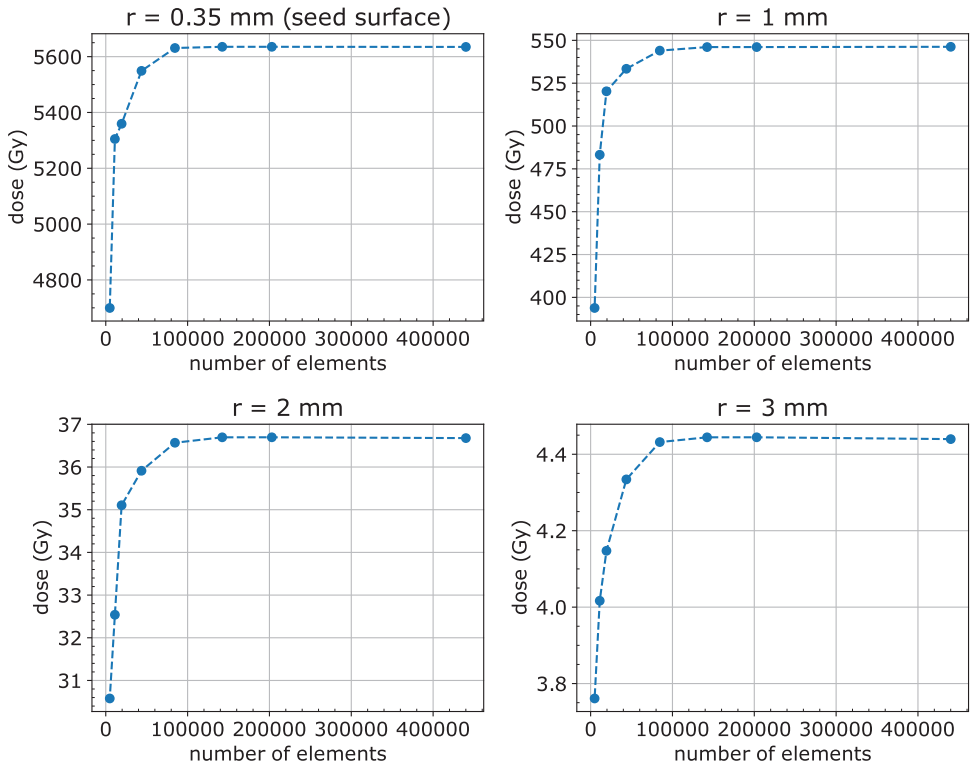

FIGURE 5 Convergence of source midplane solution with element size. Accumulated dose after 30 days at $r = 0.35, 1, 2$, and 3 mm, as a function of the number of elements in the mesh.

In our work, we reformulate the D-L equations into finite element variational statements and calculate the dose profiles in two slices perpendicular and parallel to the source axis. The two previously existing approaches for solving the D-L equations make use of finite difference schemes.[15] Our approach differs from these in two key respects. The first is in the method by which the system of partial differential equations is converted into a system of linear equations. In finite difference schemes, the spatial gradients and time derivatives are approximated by differences between neighboring mesh elements. The solution of the linear system is a vector of the approximated number density values at each element. In our approach, the spatial derivatives are not discretized. Instead, the system of differential equations is reformulated into a variational statement that is solved exactly. The solution is a basis expansion over a set of functions that are continuous over the entire domain. The second key difference is in the formation of the mesh. The DART1D mesh is made up of line segments of a fixed size; similarly, its extension DART2D uses rectangular elements of fixed size.[15] The discretization of spatial gradients required by finite difference approaches makes the implementation of non-rectangular meshes with varying element size and orientation extremely difficult. FEM makes possible the use of an unstructured mesh, allowing us to locally increase the element density, as well as more tightly conform element edges to irregularly shaped domains.

Compared to the previous method, our approach tends to predict higher doses in the source midplane close to the source wall and lower doses along the source axis close to the source ends. The trend in the midplane is consistent with a dose calculation by the authors of DART2D using COMSOL, which showed that DART2D underestimates the dose close to the source by around 1.4%.[15] To our knowledge, no analogous COMSOL validation has been published for the axial dose profile. Because of the local mesh refinement used in FEM, the large gradients in these areas can approximated with a higher point density. A denser mesh is generally more accurate in approximating solutions with large gradients.[18] The doses close to the source are well above the 10 Gy necessary for effective cell killing, so the clinical impact of these differences may be small. Beyond 0.5, the FEM calculation method produces dose profiles within 1% of DART1D and DART2D at clinically relevant distances from the source. The most salient advantage of using FEM over previous approaches is the intrinsic ability to scale for inhomogenous and time-dependent geometries. The diffusion properties of tumor tissue vary on a macroscopic scale with implications relevant for treatment planning. For example, the ^{212}Pb leakage probability is higher near the tumor edge where there is more vasculature that it is in the interior. As a result, calculations using fixed meshes must set the diffusion lengths and clearance rates at conservative values so that a minimum dose is guaranteed in the

24734209, 0, Downloaded from https://aapm.onlinelibrary.wiley.com/doi/10.1002/mp.16803 by Eliran Ron - Cochrane Israel , Wiley Online Library on [07/11/2023]. See the Terms and Conditions (https://onlinelibrary.wiley.com/terms-and-conditions) on Wiley Online Library for rules of use; OA articles are governed by the applicable Creative Commons License

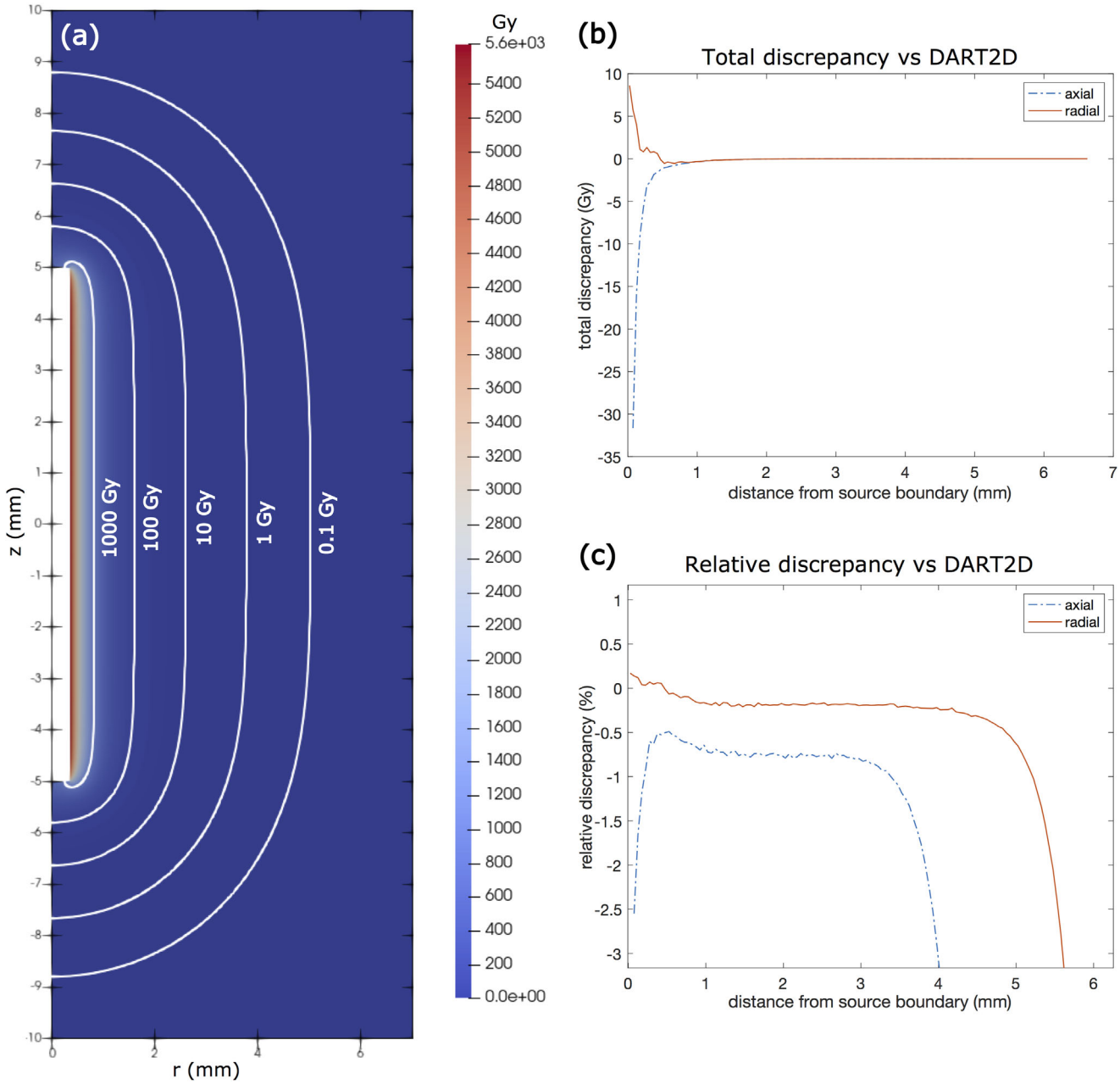

FIGURE 6 Total alpha particle dose obtained for the axial geometry with FEM and compared to DART2D. (a) Total dose in the plane intersecting the central axis of the source. (b) Discrepancy between the FEM-calculated dose and the dose calculated using DART2D as a function of distance from the source along the radial ($z = 0$mm) and axial ($r = 0.35$mm) directions. (c) Relative discrepancy between the FEM and DART2D doses along the radial and axial directions. FEM, finite element method, DART, diffusing alpha-emitters radiation therapy.

outer regions, although the dose in other regions will be higher than predicted.[16]

We emphasize that the results presented here serve only as a solution to the D-L model up to the choice of physical parameters. In Section 3.2, we discuss changes in the alpha dose profiles in the source midplane for different values of the diffusion lengths, clearance rate, and desorption probabilities. Ranges for these parameters taken from literature are large,[1,14,22,23] and the experimental determination of diffusion lengths and clearance rates, though outside the scope of this work, remains an important task for estimating the dose delivered in realistic treatment scenarios.[14] Previous work investigated the effect of diffusion parameter values and uncertainties on the necessary source activity and spacing required to achieve 10 Gy at the location of minimum dose in a lattice of sources.[16] These results and the current work both suggest that the dominant contributors to the dose profile are the ^{220}Rn and ^{212}Pb diffusion lengths, with the ^{212}Pb leakage probability as a secondary effect.

An important drawback to the current implementation is the computational resources it requires. For the

24734209, 0, Downloaded from https://aapm.onlinelibrary.wiley.com/doi/10.1002/mp.16803 by Eliran Ron - Cochrane Israel , Wiley Online Library on [07/11/2023]. See the Terms and Conditions (https://onlinelibrary.wiley.com/terms-and-conditions) on Wiley Online Library for rules of use; OA articles are governed by the applicable Creative Commons License

mesh and parameters described in Section 2.3, one run of our code finishes in five hours. The majority of this time is spent solving the 440 000-by-440 000 linear system in Equation 24. In this work, we have used sparse LU decomposition, which is optimal for smaller systems, but becomes time-consuming and memory-intensive for systems with more than a few thousand elements. Using an iterative solver with preconditioning is one avenue for improving the efficiency of our code.[17] In the current implementation, the radii defining successive refinement zones and number of refinement steps is hardcoded in the program. The addition of adaptive mesh refinement, in which the local mesh density is automatically refined in each time step based on a local error estimate,[17] would greatly streamline the meshing process for different tissue parameters and geometries. In addition to computational considerations, moving beyond the assumptions of the D-L model is important for modeling realistic dose deposition. Accurate calculations of the dose will need to take into account diffusion properties that change in space and time as treatment progresses. Additionally, the tumor can shrink and the sources may come closer together as necrotic tissue is cleared away,[5] necessitating time-dependent domain boundaries. Finally, future work will be performed to incorporate healthy and necrotic subdomains with appropriate physical parameters and boundary conditions to handle cases with tissue-to-air boundaries.

5 | CONCLUSIONS

We implemented a FEniCS-based FEM program to solve the D-L model on a two-dimensional domain in the source midplane and axial plane. At clinically relevant distances, the calculated total dose in the source midplane after 30 days of treatment agrees with that obtained using DART1D and DART2D to within 1%; initial calculations of the dose profile in the axial plane of the source show a difference of 3% along the source axis compared to DART2D. The largest differences occur in areas where the dose changes rapidly with distance. In these regions, the local mesh refinement made possible by an unstructured FEM mesh is potentially better able to approximate high gradients. In the source midplane at the midpoint of the recommended seed spacing of 2 mm, the dose may vary by over a factor of 3 depending on the choice of parameter values. Therefore, more experimental data on the diffusion properties of various tumor tissues is needed to refine the range of likely values in realistic treatment scenarios. The approach outlined in this paper will be extended to account for more complicated non-symmetric geometries in two dimensions, including tissue-to-air interfaces, as well as spatial inhomogeneity and time dependence in tissue parameters.

ACKNOWLEDGMENTS

We thank Guy Heger and Lior Arazi for sharing example dose profile data calculated by DART2D, which expedited the comparisons in Section 3.4 This study was supported in part by NCI P30 CA008748. This work was partly funded by Alpha TAU Medical Ltd (ATM).

CONFLICT OF INTEREST STATEMENT

The authors have no relevant conflicts of interest to disclose.

DATA AVAILABILITY STATEMENT

The code and resulting data generated for this work are available upon request to the corresponding author.

REFERENCES

1. Arazi L, Cooks T, Schmidt M, Keisari Y, Kelson I. Treatment of solid tumors by interstitial release of recoiling short-lived alpha emitters. *Phys Med Biol*. 2007;52:5025.
2. Cooks T, Schmidt M, Bittan H, et al. Local control of lung derived tumors by diffusing alpha-emitting atoms released from intratumoral wires loaded with radium-224. *Int J of Rad Oncol Biol Phys*. 2009;74:966-973.
3. Cooks T, Tal M, Raab S, et al. Intratumoral 224Ra-loaded wires spread alpha-emitters inside solid human tumors in athymic mice achieving tumor control. *Anticancer Res*. 2012;32:5315-5321.
4. Keisari Y, Popovtzer A, Kelson I. Effective treatment of metastatic cancer by an innovative intratumoral alpha particle-mediated radiotherapy in combination with immunotherapy: a short review. *J Phys: Conf Ser*. 2020;1662:012016.
5. Popovtzer A, Rosenfeld E, Mizrachi A, et al. Initial safety and tumor control results from a "First-in-Human" multicenter prospective trial evaluating a novel alpha-emitting radionuclide for the treatment of locally advanced recurrent squamous cell carcinomas of the skin and head and neck. *Int J of Radiat Oncol Biol Phys*. 2020;106:571-578.
6. NuDat 3.0. Upton, NY: National Nuclear Data Center; 1996, Updated April, 2022. Accessed September 22, 2023. https://www.nndc.bnl.gov/nudat3/
7. Cooks T, Arazi L, Efrati M, et al. Interstitial wires releasing diffusing alpha emitters combined with chemotherapy improved local tumor control and survival in squamous cell carcinoma-bearing mice. *Cancer* 2009;115:1791-1801.
8. Horev-Drori G, Cooks T, Bittan H, et al. Local control of experimental malignant pancreatic tumors by treatment with a combination of chemotherapy and intratumoral 224Radium-loaded wires releasing alpha-emitting atoms. *Transl Res*. 2012;159:32-41.
9. Reitkopf-Brodutch S, Confino H, Schmidt M, et al. Ablation of experimental colon cancer by intratumoral 224Radium-loaded wires is mediated by alpha particles released from atoms which spread in the tumor and can be augmented by chemotherapy. *Int J Radiat Biol*. 2015;91:179-186. PMID: 25179346.
10. Confino H, Hochman I, Efrati M, et al. Tumor ablation by intratumoral Ra-224-loaded wires induces anti-tumor immunity against experimental metastatic tumors. *Cancer Immunol Immunother*. 2015;64:191-199.
11. Confino H, Schmidt M, Efrati M, et al. Inhibition of mouse breast adenocarcinoma growth by ablation with intratumoral alpha-irradiation combined with inhibitors of immunosuppression and CpG. *Cancer Immunol Immunother*. 2016;65:1149-1158.
12. Domankevich V, Cohen A, Efrati M, et al. Combining alpha radiation-based brachytherapy with immunomodulators promotes complete tumor regression in mice via tumor-specific long-term immune response. *Cancer Immunol Immunother*. 2019;68:1949-1958.

24734209, 0, Downloaded from https://aapm.onlinelibrary.wiley.com/doi/10.1002/mp.16803 by Eliran Ron - Cochrane Israel , Wiley Online Library on [07/11/2023]. See the Terms and Conditions (https://onlinelibrary.wiley.com/terms-and-conditions) on Wiley Online Library for rules of use; OA articles are governed by the applicable Creative Commons License

13. Domankevich V, Efrati M, Schmidt M, et al. RIG-1-like receptor activation synergizes with intratumoral alpha radiation to induce pancreatic tumor rejection, triple-negative breast metastases clearance, and antitumor immune memory in mice. *Front Oncol*. 2020;10:990.
14. Arazi L. Diffusing alpha-emitters radiation therapy: approximate modeling of the macroscopic alpha particle dose of a point source. *Phys Med Biol*. 2020;65:015015.
15. Heger G, Roy A, Dumančić M, Arazi L. Alpha dose modeling in diffusing alpha-emitters radiation therapy. Part I: single-seed calculations in one and two dimensions. *Med Phys*. 2023;50:1793-1811. https://doi.org/10.1002/mp.16145
16. Heger G, Dumančić M, Roy A, Arazi L. Alpha dose modeling in Diffusing alpha-emitters Radiation Therapy. Part II: lattice studies. *Med Phys*. 2023;50:1812-1823. https://doi.org/10.1002/mp.16155
17. Larson MG, Bengzon F. *The Finite Element Method: Theory, Implementation, and Applications*. Springer; 2013.
18. Reddy JN. *Introduction to the Finite Element Method*. McGraw Hill Education; 1993.
19. Langtangen HP, Logg A. *Solving PDEs in Python: The FEniCS Tutorial I, volume 3 of Simula SpringerBriefs on Computing*. Springer Open; 2016.
20. Alnæs M, Blechta J, Hake J, et al. The FEniCS Project Version 1.5. Archive of Numerical Software. *IWR, Universität Heidelberg*. 2015;3(100):9-23.
21. Logg A, Mardal K-A, Wells G. Automated solution of differential equations by the finite element method: the fenics book. *Volume 84 of Lecture Notes in Computational Science and Engineering*. Springer; 2016.
22. Jähne B, Heinz G, Dietrich W. Measurement of the diffusion coefficients of sparingly soluble gases in water. *J Geophys Res*. 1987;92:10767-10776.
23. Council NR, *Risk Assessment of Radon in Drinking Water*. The National Academies Press; 1999.
24. Feliciani G, Bellia SR, Del Duca M, et al. A new approach for a safe and reproducible seeds positioning for diffusing alpha-emitters radiation therapy of squamous cell skin cancer: a feasibility study. *Cancers*. 2022;14:240.
25. D'Andrea MA, VanderWalde NA, Ballo MT, et al. Feasibility and safety of diffusing alpha-emitter radiation therapy for recurrent or unresectable skin cancers. *JAMA Netw Open*. 2023;6:e2312824-e2312824.

SUPPORTING INFORMATION

Additional supporting information can be found online in the Supporting Information section at the end of this article.

How to cite this article: Zhang IP, Cohen GN, Damato AL. A finite element method for modeling diffusion of alpha-emitting particles in tissue. *Med Phys*. 2023;1-14. https://doi.org/10.1002/mp.16803

24734209, 0, Downloaded from https://aapm.onlinelibrary.wiley.com/doi/10.1002/mp.16803 by Eliran Ron - Cochrane Israel , Wiley Online Library on [07/11/2023]. See the Terms and Conditions (https://onlinelibrary.wiley.com/terms-and-conditions) on Wiley Online Library for rules of use; OA articles are governed by the applicable Creative Commons License